Sliding wear resistance and residual stresses of parts repaired by laser metal deposition

Théo Zurcher, Itziar Serrano-Munoz, Tatiana Mishurova, Guilherme Abreu Faria, Sebastian Degener, Vincent Fridrici, Eric Charkaluk, Giovanni Bruno

Sliding wear resistance and residual stresses of parts repaired by Laser Metal Deposition

Théo Zurcher [1,4,*], Itziar Serrano-Munoz[2], Tatiana Mishurova[2], Guilherme Abreu Faria[3], Sebastian Degener[3], Vincent Fridrici[4], Eric Charkaluk[1*], and Giovanni Bruno[2,5]

[1]Ecole Polytechnique, Laboratoire de Mécanique des Solides, UMR CNRS 7649, Palaiseau, 91120, France

[2]Bundesanstalt für Materialforschung und -prüfung, Unter den Eichen 87, Berlin 12205, Germany

[3]Helmholtz-Zentrum Hereon, Institute of Materials Physics, 21502 Geesthacht, Germany

[4]Ecole Centrale de Lyon, Laboratoire de Tribologie et Dynamique des Systèmes, UMR CNRS 5513 ECL-ENTPE, Ecully, 69130, France

[5]University of Potsdam, Institute of Physics and Astronomy, Karl-Liebknecht-Straße 24/25, Potsdam 14476, Germany

[*]Corresponding author: theo.zurcher@polytechnique.edu, eric.charkaluk@polytechnique.edu

Abstract

Large temperature gradients inherent to additive manufacturing (AM) processes induce large residual stress (RS) in the final part. Because RS can influence the tribological properties, this study focuses on the relationship between wear sliding properties and RS in IN718 coatings. Such coatings were deposited with a Laser Metal Deposition (LMD) machine using to two different scanning strategies. The wear resistance and RS state of two types of samples were investigated after surface milling. RS were measured before and after tests on a reciprocating sliding test apparatus. Two different X-ray diffraction techniques were employed to measure the surface and subsurface state RS: Laboratory Energy Dispersive X-ray Diffraction (LEDXD) and Synchrotron X-ray Energy Dispersive Diffraction (SXEDD). Due to the milling process, coatings show similar depth distributions of RS from 22 µm to 92 µm depth, but exhibit different magnitudes depending on the scanning strategy used. Reciprocating sliding wear tests induced high compressive residual stresses that erased the initial RS state. However, a similar wear behavior was observed in the two samples, which possess similar texture and microstructure. This demonstrates that the influence of RS on wear resistance is a second-order effect. Nevertheless, it was observed that RS can still impact the wear performance at the early testing stages of the repaired parts.

Keywords: Residual stress, Additive manufacturing, Laser Metal Deposition, Wear, Tribology

1. Introduction

Repair of worn metallic parts is a convenient way to extend the life of resource-intensive and critical mechanical components, such as the wheels used in train bogies. Typically, subtractive methods are used to recondition damaged parts [1]. However, the main drawback of these methods is the limited number of refurbishments before parts need to be discarded. Alternatively, the damaged area can also be refilled. A number of conventional additive techniques are already used to achieve restoration [2], [3]. Laser Metal Deposition (LMD) is an additive manufacturing (AM) process that allows the manufacture, modification and repair of 3D geometries [4]. LMD uses powder feedstock material that is molten by a high-energy laser beam. The melt pool created by the laser beam is constantly fed with powder along the processing direction. A rapid solidification of the newly deposited material ensues after the laser pass. This process induces the development of high thermal gradients. Three-dimensional builds are manufactured by depositing beads next to and/or on top of each other. The main advantage of this technology is its capacity to accurately repair parts in an automated, computer controlled way [5]. Contrary to conventional methods, LMD allows repairs with a small heat-affected zone (HAZ) and high repeatability [6]. Moreover, LMD can deposit different types of material grades, providing that the grades possess good weldability [7]. IN718 processed by LMD is one of the most studied alloys and is widely used in the aerospace industry for its good mechanical

properties at high temperatures (up to 650°C [8]) and its good corrosion resistance. For instance, some authors have studied the ability of LMD process to repair turbine blades commonly used in aircraft engines [9]–[11].

One of the main drawbacks of the LMD process is the presence of high residual stress (RS) inside the repaired parts. If unmanaged, RS can distort parts [12] or, in the worst cases, cause premature cracking and delamination of the repair [13]. In AM, RS is primarily resulting from the high magnitude and localized thermal gradient induced by the laser beam [14]. The RS state can prove highly deleterious to the mechanical resistance of components: the RS can add to the load applied on the component, resulting in an unexpected failure [15], [16]. However, this also implies that, with a suitable post-processing, harmful RS can be removed, or even beneficial RS can be purposely introduced. The impact of RS on mechanical properties [17], [18] and the optimization of process parameters to mitigate them [19]–[21] have been already largely studied in the literature. From a mechanical point of view, one of the criteria for a good repair is that the reconditioned part has wear-resistance comparable to the pristine part. However, RS induced by the LMD process could negatively impact the wear properties of the repaired part. For conventionally produced materials, it has been reported that compressive RS at the surface may reduce the sliding wear of metallic alloys [22], [23]. To the best of our knowledge, up to date there are no studies investigating how LMD-induced RS impacts the wear sliding resistance.

The study of the wear of parts manufactured by AM was focused on the wear resistance of Laser Powder Bed Fusion (LPBF) rather than on the LMD process. Generally, parts produced via Laser Powder Bed Fusion (LPBF) exhibit improved wear resistance properties compared to parts manufactured via conventional processes. Due to an increased hardness localized at the cell walls, the cellular sub-microstructure specific to AM materials can highly improve the wear properties [24]. As a rule of thumb, the higher the hardness, the lower the wear. Therefore, an accelerated work-hardening effect caused by the initial high density of dislocations tends to decrease the wear rate of AM parts. In addition, several articles showed that grain orientation has a substantial impact on wear [25], [26]. In fact, the amount of High Angle Grain Boundaries (HAGB) encountered by the counter-body can also influence the wear results [26]. Because LMD materials have some microstructural features in common with the LPBF materials, a good wear resistance of the LMD repairs might be expected.

This work aims at elucidating the influence of RS on the wear properties of IN718 parts repaired by LMD. Samples produced using two different scanning strategies are investigated. To mimic a real repaired part, the as-built samples surface is milled prior to the wear tests. We focus our study on the RS state before and after reciprocating sliding wear tests. Laboratory Energy Dispersive X-ray Diffraction (LEDXD) and Synchrotron X-ray Energy Dispersive Diffraction (SXEDD) techniques are used to obtain surface and subsurface RS, respectively. In addition, the microstructure is analyzed by means of scanning electron microscopy (SEM) and electron backscatter diffraction (EBSD), the porosity content is evaluated via optical microscopy, and the hardness is measured using Vickers indentation. This comprehensive investigation allows us to rationalize the interplay between wear resistance and RS in terms of the LMD scanning strategy.

2. Material & Methods

2.1. Manufacturing of LMD samples

The samples were manufactured using a *BeAM* (Cebazat, France) DED mobile machine. This AM machine is equipped with a 500 W YLR-fiber laser with a laser spot diameter of 0.74 mm. As feedstock material, an IN718 gas-atomized powder provided by Oerlikon (Barleben, Germany) was used. The chemical composition of the powder is given in Table 1.

Elements	Ni	Fe	Ti	Al	Nb	Co	Cr	Mo	Mn	C	N	Si
Weight%	Bal.	18.25	0.92	0.42	5.15	0.05	18.92	3.11	0.1	0.05	0.03	0.03

Table 1. Chemical composition of the IN718 powder used in this study.

The sample geometry is shown in Fig. 1a. The sample consisted of an 85×65×8 mm plate made of XC48 steel substrate on which a 55×55×2 mm IN718 repair coating was deposited by LMD. As shown in Fig. 1b,c, the repaired area was deposited with two different scanning strategies: namely, Strat 0° and Strat 67°. The Strat 0° samples were manufactured using a back-and-forth laser path parallel to the Y direction. No rotation (between different layers) of the laser path direction was made along the building direction. The first layer of the Strat 67° sample was also deposited with a laser path along the Y direction.

However, in this case, an incremental rotation of 67° of the laser path direction was implemented along the building direction (at each layer).

Apart from the scanning strategy, all the samples were built with the same process parameters: a laser power of 325 W, a powder rate flow of 7 g/min, a scanning speed of 2250 mm/min, and a track overlap of 30%. Finally, to perform tribological tests mimicking industrial conditions (low roughness), the samples were milled using the parameters given in Table 2. All the samples were milled in the same direction (i.e., parallel to the Y direction), as indicated in Fig. 1a. The final roughness was measured with an interferometer at four different locations, resulting in Sa = 0.70 ± 0.04 µm.

Milling parameters						
Material of flutes	Number of flutes	Reamer diameter (mm)	Spindle rotation speed (rpm)	Cuting speed (mm/min)	Depth of cut (mm)	Depth of cut for the finishing stage (mm)
Carbide	7	80	95	29	0.2	0.1

Table 2. Summary of the milling parameters used in this study. In total, 0.5 mm of the original coating height was removed.

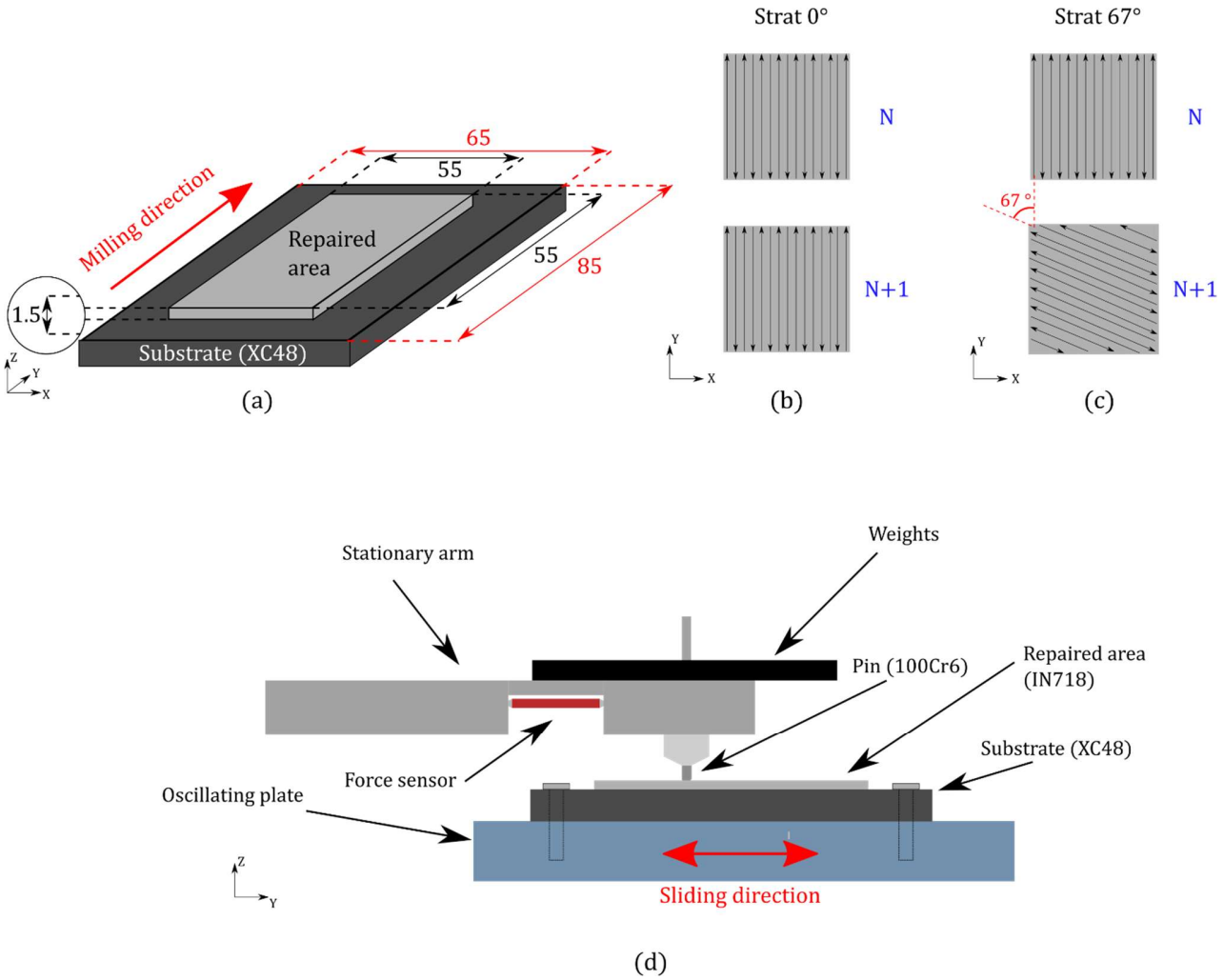

Fig. 1 (a) Geometry of the sample. Dimensions are shown in millimeters. LMD scanning strategies corresponding to (b) the Strat 0° sample and (c) the Strat 67° sample. (d) Schematics of the reciprocating sliding test bench

2.2. Material characterization

Electron Backscatter Diffraction (EBSD) analyses were performed on unworn samples. Samples were first ground using SiC paper starting from a grit of 400 down to 4000. Subsequently, they were polished using 3 and 1 µm diamond slurries for 1 min each. Finally, to improve the quality of Kikuchi patterns and to suppress the distortion induced by the previous polish, the samples were subjected to an ion-polishing protocol, which consisted of focusing an argon ion beam on the polished surface with an incidence angle of 9°. The energy on the ion beam was set to 6 keV, and the samples had a rotation speed of 6 rpm. EBSD maps were acquired using an *FEI Quanta 600F* SEM equipped with an EBSD camera from *Oxford Instruments* [27]. All maps were acquired using the same parameters. Each pixel had a dimension of 0.6×0.6 µm. The acquired data were treated with *Aztec* and *Channel5* software supplied by *Oxford Instruments*. The grain boundary threshold was set at 10°. The Grain Average Misorientation (GAM) map (in Fig. 3) was determined by averaging the local misorientation within each grain, using only the first neighbors for the calculation.

The porosity was measured below the wear profile of the two samples (Fig. 4). After being polished, digital microscope images with a magnification of ×200 were acquired and stitched together. Finally, the porosity *area* fraction was calculated by image analysis using *ImageJ* free software [28]. Each point of the curve plotted in Fig. 4b,d corresponds to the porosity inside an area of 1.8×1.4 mm².

A hardness profile was obtained on one of the Strat 67° sample, starting from the right edge and moving to the center of the sample. The measurement was performed using a *Zwick* micro-indenter [29]. It consisted of a matrix of 27×3 indents. In the X direction, each of the 27 points were separated by 1 mm, and 3 indentations were done (each of them separated by 100 µm). The indentation procedure consisted of applying a normal load of 750 mN for 5 seconds. The average length of the diagonals of the indents was 20 µm.

2.3. Synchrotron XRD measurements

Synchrotron X-Ray Energy Dispersive Diffraction (SXEDD) measurements were performed at the P61A beamline of the PETRA III synchrotron (Deutsches Elektronen-Synchrotron, Hamburg, Germany), dedicated to Materials Science and Engineering. The beamline features a white beam with an energy range from 30 to 200 keV [30]. The two detectors available are equipped with 0.5 m long slit collimators. The location of the measurement points is shown in Fig. 5. The measurements were performed in reflection mode. By rewriting the Braggs law using the photon energy (Equation 1), the lattice spacing d^{hkl} can be calculated as function of the energy.

$$d^{hkl} = \frac{6.199}{\sin\theta} \cdot \frac{1}{E^{hkl}} \quad (1)$$

With E^{hkl} being the energy and θ the diffraction angle, respectively.

The use of a white beam allows accessing the lattice spacing at several depths, τ^{hkl}, as a function of the corresponding reflections. The depth is calculated using Equation 2 (where ψ is the specimen tilt angle)

$$\tau^{hkl} = \frac{\sin\theta}{2\mu(E^{hk})} \cdot cos\psi \quad (2)$$

$\mu(E^{hkl})$ is the absorption coefficient, dependent on the energy E^{hkl}. The specific $\mu(E^{hkl}_{IN718})$ was calculated by considering all the alloying elements in IN718 using the equation 3.

$$\frac{\mu(E^{hkl}_{IN718})}{\rho} = \sum_i w_i \left(\frac{\mu(E^{hkl})}{\rho}\right)_i \quad (3)$$

With w_i being the mass fraction of the alloying element *i* and $(\frac{\mu(E^{hk})}{\rho})_i$ the mass-energy absorption coefficient of the latter for a given energy [31].

The evaluation of the RS was restricted to the lattice spacings of the 311 and 422 reflections. These reflections are used because they do not accumulate high intergranular stress [32], i.e. their response to stress well reflects the macroscopic sample response. To probe several depths, three different diffraction angles were used: 2θ = 5°, 8°, and 12°. With these diffraction angles, the depth values for the {311} planes were τ^{311} = 64 μm, 43 μm, and 22 μm, respectively. To gain information from higher depths, the 422 reflection was used only for the 8° diffraction angle, corresponding to 92 µm depth. The 422 reflection at 2θ = 5° yielded poor intensities and did not yield a reliable evaluation of the strain. In the case of 2θ = 12° , the 422 reflection probes an average depth of 45 µm; at such depth, the strain values would overlap with those obtained with 2θ = 8° for the {311} planes.

The RS was calculated by using the $sin^2\psi$ method [33], assuming that the RS in the direction normal to the probed surface is negligible (i.e., in-plane biaxial stress field condition). To this aim, the samples were mounted on a Eulerian cradle. A total of 19 ψ (tilt) angles were investigated for a given φ direction. Two φ directions (φ = 0° and φ = 90°) were employed, in order to determine the RS in the X and Y directions. The reader is referred to Fig.2 for the definition of the angles.

By using the fundamental equations of X-Ray stress analysis for the two values of φ, we obtain:

$$\varepsilon_{0,\psi} = \frac{1}{2}S_2\sigma_X sin^2\psi + S_1(\sigma_X + \sigma_Y) \quad (4)$$

$$\varepsilon_{90,\psi} = \frac{1}{2}S_2\sigma_Y sin^2\psi + S_1(\sigma_X + \sigma_Y) \quad (5)$$

As the $sin^2\psi$ plots show a liner relationship for both the 311 and 422 reflections. No significant ψ-splitting can be observed, so that the shear stresses are considered negligible [34]. The Diffraction Elastic Constants (DEC) used in equation 4 and 5 are given in Table 3. These DECs were calculated by applying the Reuss model [35] using the single crystal constants of an IN718 alloy reported in Haldipur et al. [36]. The RS values were computed using a free access in-house python code developed at P61A beamline. The peaks were fitted using a Pseudo-Voigt function (the background determined by interpolation). The experimental setup is depicted in the Fig. 2a. In the case of the wear tracks, only the X component of the RS (φ = 0°, i.e., parallel to the longitudinal dimension of the track) was measured because of the elongated shape of the gauge region. Each RS value shown for one double wear track in Fig. 7 is the average of two acquisitions. The value of the reference points in the graphs is the mean value of the three measurement points illustrated in Fig. 7a.

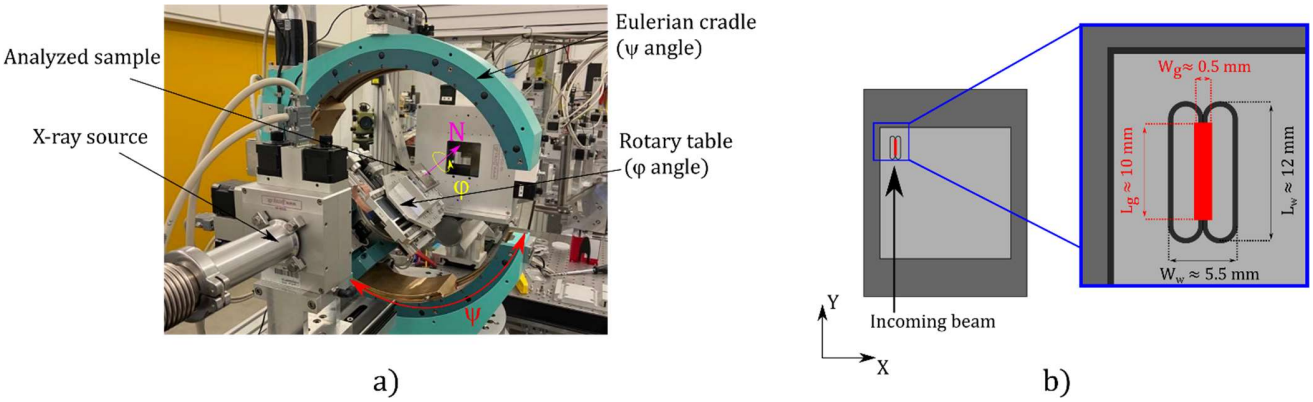

Fig. 2 (a)Synchrotron XRD experimental setup. (b) Scheme of the gauge volume probing the X-direction of strain, i.e. with φ = 0° (not to scale). If one were to probe the Y strain direction, the gauge volume would extend over the whole track and beyond; one would therefore lose spatial resolution.

2.4. Laboratory XRD measurements

Laboratory Energy Dispersive X-ray Diffraction (LEDXD) was performed with a LIMAX-70 instrument located at the X-Ray CoreLab of Helmholtz Zentrum Berlin (HZB), Germany. This instrument uses a metal jet source [37] with a maximum energy

of 70 keV. Also in this case, the $sin^2\psi$ method was used to calculate the RS, as the instrument is also equipped with a Eulerian cradle. In total, 9 ψ angles were probed in a range from 0° to 63° for two φ directions (0° and 90°, corresponding to the X and Y axes, respectively). Seven measurement points over the samples surface were investigated (see Fig. 5). The diffraction angle was set to 2θ = 16.6°, which corresponds to a depth of 17 μm for the 311 reflection. Data processing was carried out using the in-house developed EDDIDAT [38] software. The diffraction peaks were fitted using a Pseudo-Voigt function. The diffraction elastic constants used are those shown in Table 3 and the computed RS corresponds to the 311 reflection.

Crystallographic reflection planes, hkl	S_1 ($MPa^{-1} \times 10^{-6}$)	$\frac{1}{2}S_2$ ($MPa^{-1} \times 10^{-6}$)
311	1.831	7.409
422	1.37	6.027

Table 3. DECs calculated using the Reuss model.

2.5. Wear tests

The reciprocation wear bench test was entirely designed and built at the LTDS laboratory (Ecole Centrale de Lyon, France). The device is shown in Fig. 1 d. Each wear test consisted in putting a 100Cr6 pin in contact with the surface of the samples. The material of the pin was chosen for its high hardness (around 840 HV), which ensures that wear occurs mainly on the tested sample. The pin had a diameter of 3 mm with fillets of 0.5 mm radius at its extremities. The tribological parameters are summarized in Table 4. Prior to each test, the pin was subjected to an in-situ grinding to ensure a good flat-on-flat contact between the pin and the sample surface. During the test, the friction coefficient was recorded via a tangential force sensor fixed to the stationary arm. No significant temperature increase (less than 5°C) was recorded during the wear tests. Once a test was concluded, the wear volume was measured by means of an interferometer from Bruker [39]. To reduce the uncertainty, the entire wear track surface was measured. By measuring the missing volume below the surface of the repair, the adhered debris is not considered in the wear volume.

As shown in Fig. 8, to determine the variation of the wear volume along the X position, wear tests (5,000 cycles) were performed from the right edge of the repair to its center, at every 5 mm. Those tests were performed by applying a normal load of 20 N. Subsequently, a second campaign of wear tests (*additional* 5,000 cycles) was performed inside the worn tracks. The additional wear tests required the samples to be cleaned, removing the debris inside the wear tracks by using an ethanol-soaked precision wiper. In addition, the use of new pins (also subjected to *in-situ* grinding) was necessary.

The RS measurements required the preparation of another set of samples. These samples were worn using double wear tracks with a slight overlap between them, as shown in Fig. 7. In addition, to investigate the influence of the contact stresses on the redistribution of RS, three different values of the normal loads were applied: 5, 20, and 50 N. The rest of the tribological parameters used for all the sliding tests performed in this study are summarized in Table 4.

Tribological parameters	
Normal load (N)	5, 20, or 50
Frequency (Hz)	3
Stroke length (mm)	10
Number of cycles	5,000
Temperature/Moisture content (°C/%)	20/30

Table 4. Tribological parameters used to perform the wear tests.

3. Results

3.1. Microstructure, porosity and hardness

Fig. 3a,b shows the sample co-ordinate system and a representative Grain Average Misorientation map (GAM) obtained via EBSD. This parameter gives us information on the maximum depth up to where the microstructure is impacted by the milling process. The separation line between the milled and as-built materials is considered to lay at 100 µm in depth. However, some grains below this line randomly exhibit high misorientation (> 2°). This fact can be explained by the typical sub-cellular microstructure of this alloy when manufactured by AM (shown in Fig. 3c). The sub- cells contain high dislocation density in their walls [40]. Because of a higher accumulation of dislocations within some grains, those sub-grain boundaries can be isolated as local defects with a misorientation <2° [41]. In the backscatter electron image shown in Fig 3c., the cell walls appear brighter because of the Laves phases rich in heavy elements (mainly Nb and Mo).

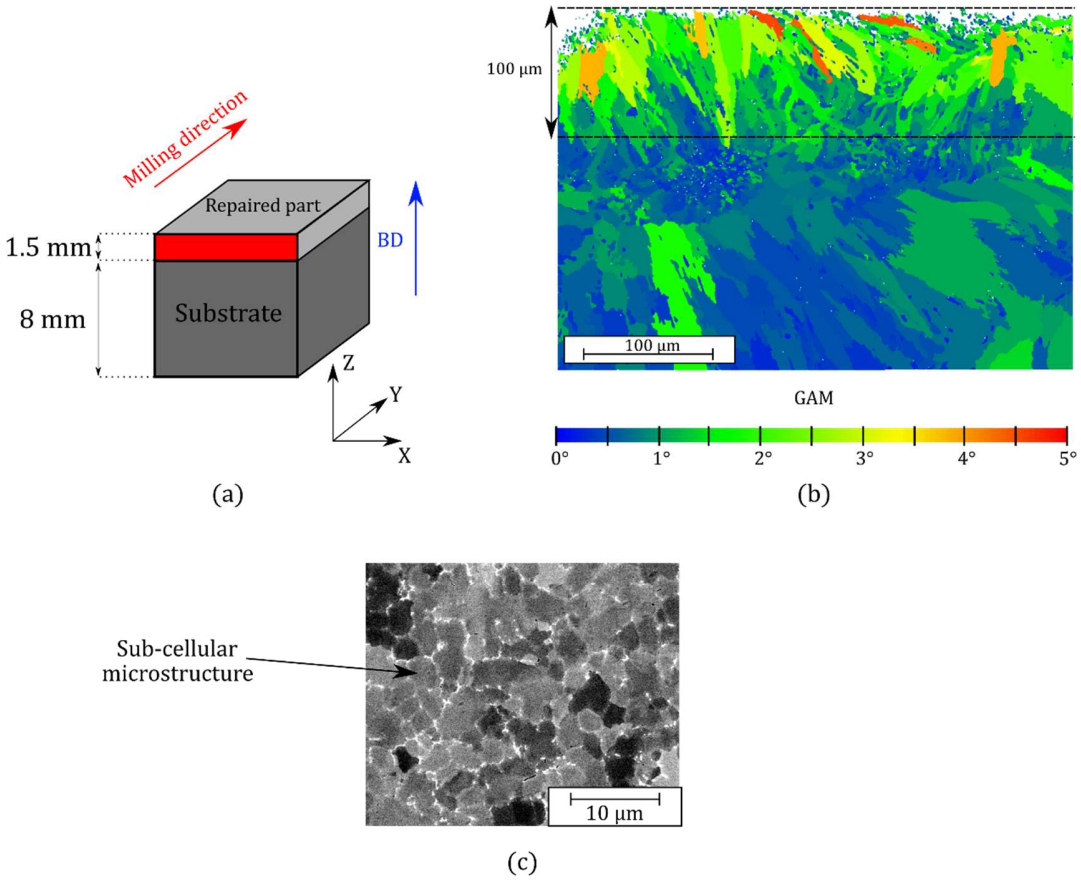

Fig. 3 (a) Schematic illustration of the height of the investigated samples. (b) EBSD map on the ZX plane of a Strat 0° sample showing the grain average misorientations (GAM). The black dashed lines indicate the boundary of the area influenced by the milling process. (c) Backscatter electron image of the sub-cellular microstructure.

Fig. 4 summarizes the material characterization analysis: the grain size was measured via EBSD on YX planes located at the center and middle-edges of the samples, whereas the porosity content and hardness were measured along the X-axis. The pole figures shown in Fig. 4a,c indicate a weak texture (the maximum of multiples of uniform density, MUD, is lower than 2) in both samples at both central and edge locations. Also, a similar heterogeneous microstructure formed by the alternation of small equiaxed grains and long columnar grains is observed at all investigated points. We can, therefore, assume that the microstructure is homogeneous across the surface of both samples. The small equiaxed grains correspond to long columnar

grains in the middle of the melt pool. Such grains grow parallel to the build direction (BD=Z). It is well known that ⟨100⟩ is the preferred solidification growth direction for cubic materials. The grain growth direction follows the maximum thermal gradient direction, which is perpendicular to the liquid/solid interface of the melt pool. Thus, seen from the top (Z direction), ⟨001⟩ grains in the middle of the melt pool are perceived as equiaxed [42], [43].

Table 5 indicates that the mean grain sizes in the middle of the repair are 24 µm and 20 µm for Strat 0° and Strat 67°, respectively. At the edge, the average grain sizes are 23 µm and 24 µm. From these results, it can be quantitatively concluded that the microstructural features do not change along the X-axis of the sample. This result is in line with the plots shown in Fig. 4b,d. The hardness profiles show no significant hardness variation between the edge and the center of the repair (along a line at mid-length). The hardness is about 310 HV for both locations. It can also be noticed in Fig. 4b,d that the porosity show the same trends. Thus, the material properties at the coating surface do not significantly vary with the position inside the sample and with the scanning strategy among samples.

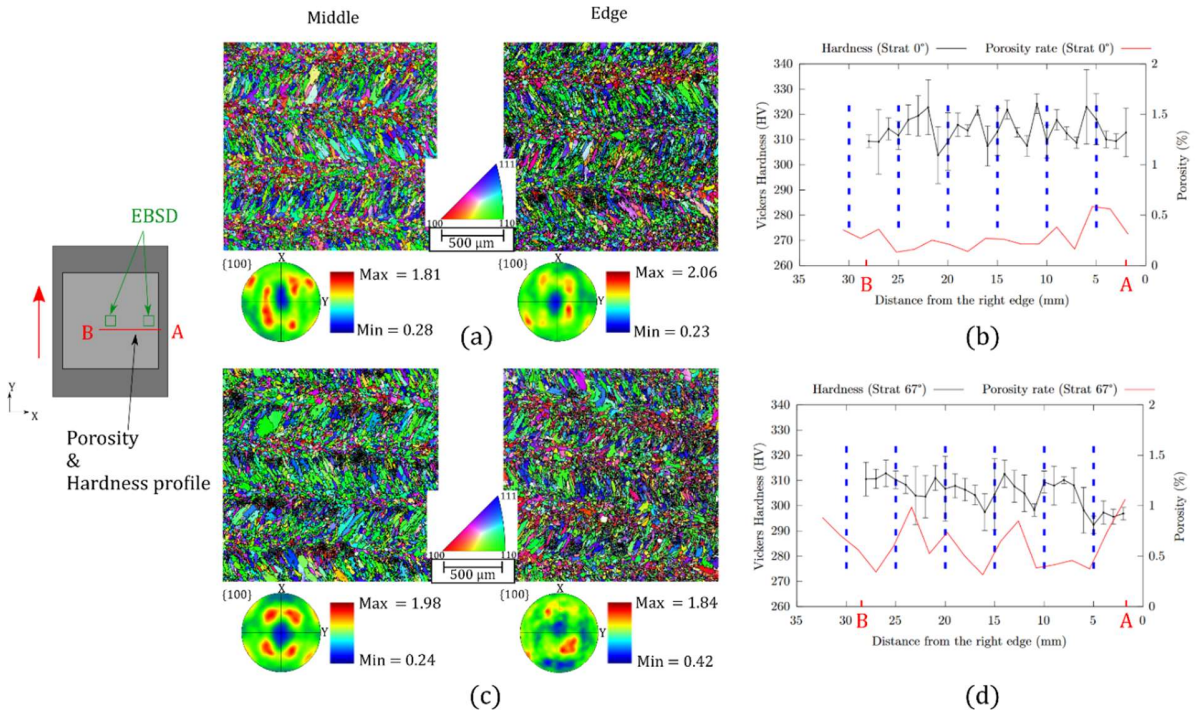

Fig. 4 EBSD orientation maps of Strat 0° (a) and Strat 67° (c) with respect to the build direction (IPF Z). Plots of the porosity and HV hardness profiles against the distance from the middle edge corresponding to Strat 0° (b) and Strat 67° (d). Vertical dotted lines in blue indicate the location of the wear tests.

Strategy	Location	Mean grain size, µm
0°	Middle	24 ± 14
	Edge	23 ± 14
67°	Middle	20 ± 11
	Edge	24 ± 16

Table 5. Mean grain size of the coating weighted by the area fraction and measured at two different locations.

3.2. RS state after milling

The spatial distributions of the RS over the XY plane, measured using LEDXD and SXEDD, are given in Fig. 5. For comparison purposes, this figure only shows the RS close to the surface (around 20 µm below the surface for both techniques). It can be observed that the results of the two techniques are similar. Moreover, the spatial distribution of RS in the two X and Y directions is the same for both investigated samples (scanning strategies). The σ_X values are lower close to the edges and the corners; they increase in the center of the samples. For Strat 0°, σ_X is always compressive, whereas for Strat 67°, σ_X changes from compressive at the edge to tensile in the center. The σ_Y values are compressive and increase from the right edge to the center. Overall, lower absolute RS magnitudes are found in Strat 67° compared to Strat 0°, as it has also been reported in the literature [20], [41].

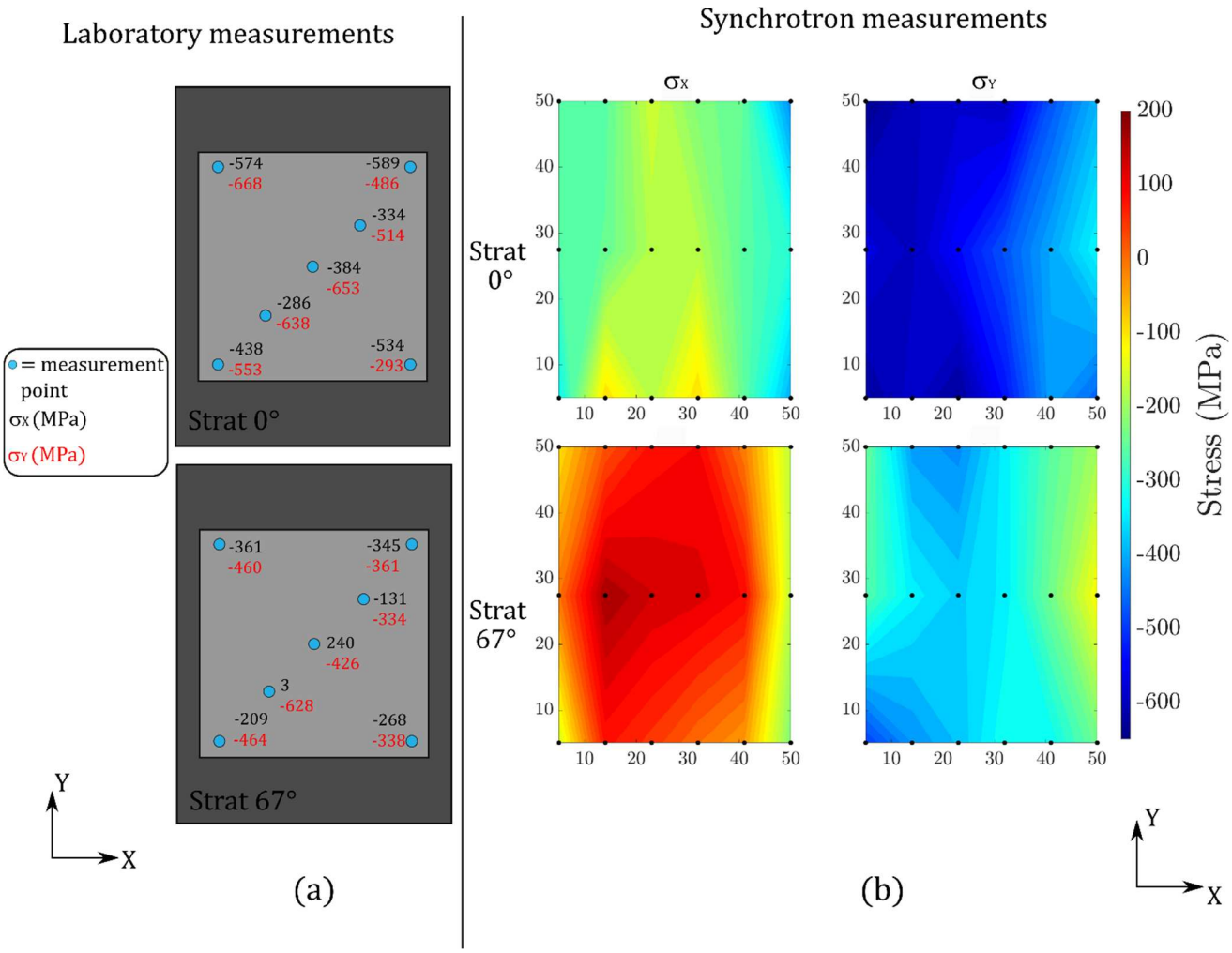

Fig. 5 Spatial distribution of the RS at about 20 µm depth for the two investigated scanning strategies obtained by (a) LEDXD and by (b) SXEDD. The blue (in (a)) and black (in (b)) dots indicate the location of the LEDXD and SXEDD measurement points. The average RS measurement errors of LEDXD and SXEDD are about 40 MPa and 15 MPa, respectively. The position (25,25) corresponds to the center of the repair. All dimensions are given in mm.

Fig. 6 shows the profile of σ_Y along the build direction (BD): the RS decreases with increasing depth (τ) for the two scanning strategies. From 22 µm to 92 µm the maximum σ_Y values go from -650 to -450 MPa for Strat 0°. For the Strat 67° sample, the decrease is less pronounced. Fig. 6 also shows that the Strat 67° sample maintains the lowest magnitude of RS with increasing depth when compared to Strat 0°. The maximum depth probed with the SXEDD technique is 92 µm, which is close to the area designated as not affected by the milling process. It is expected that the as-built material (i.e., the material

that has not been affected by the milling process) possesses a RS distribution similar to the ones measured at 92 µm depth. It can be noted that σ_X exhibits in general lower RS when compared to σ_Y.

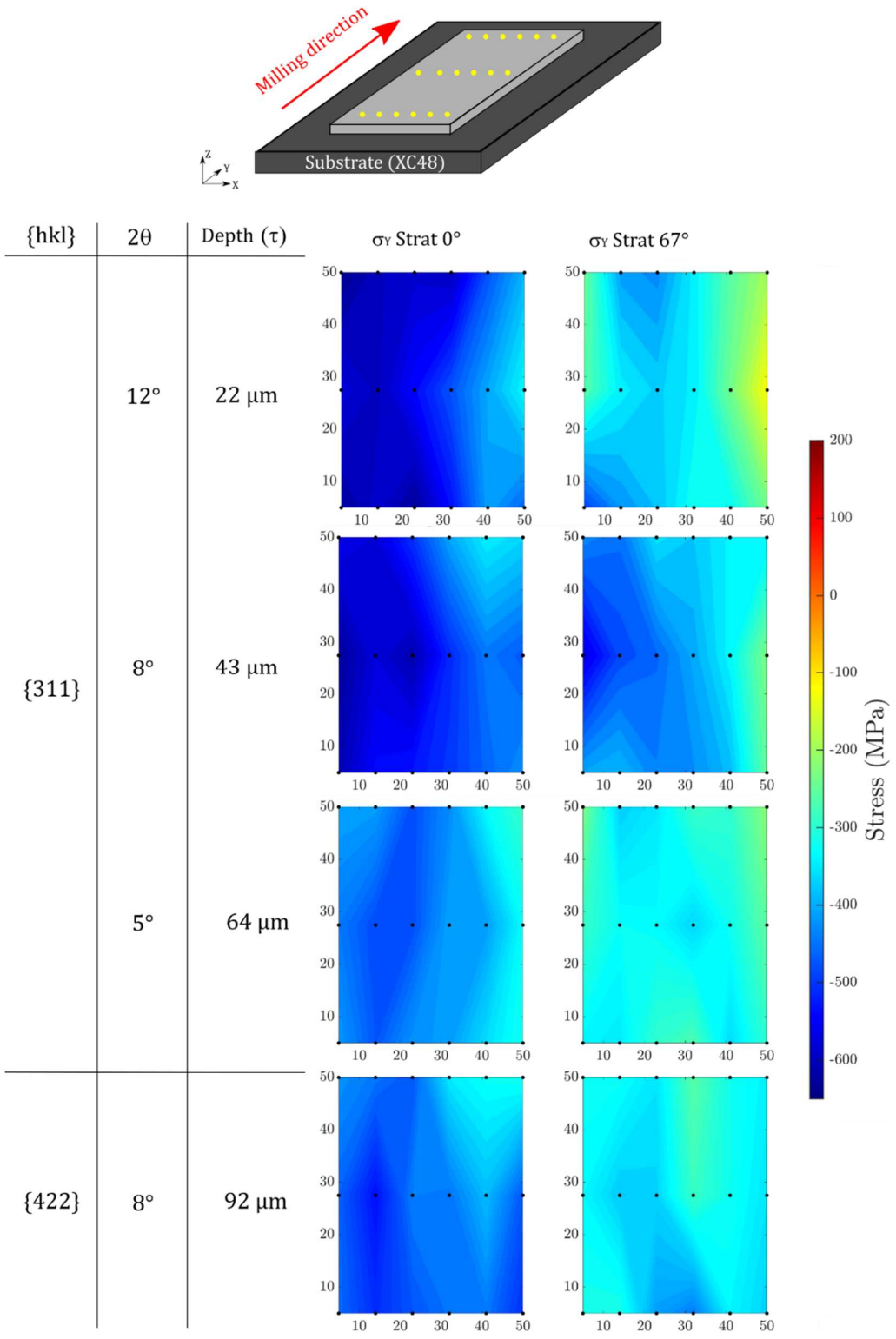

Fig. 6 YX planes showing the distribution of σ_Y as a function of depth for the two scanning strategies. The average errors are ± 20, ± 25, ± 40, and ± 40 MPa corresponding to 22, 43, 64 and 92 µm depths, respectively.

3.3. RS redistribution after sliding wear

After reciprocating sliding wear tests, RS measurements were performed within the wear tracks. Performing a double track (i.e., two single tracks with overlapping edges) instead of a single track was deemed necessary to ensure that the beam gauge is uniquely probing the worn material. Moreover, given the size of the double wear tracks (12 mm long and 5.5 mm wide), the Y stress component was not measured because the track dimensions would not allow us to uniquely probe the worn material along the X direction. The comparison of σ_X before and after wear measurements does not lose generality.

In order to investigate the impact of the normal load on the RS redistribution, three different normal forces were applied: 5, 20, and 50 N. Also, since the above results highlighted a spatial variation of the RS, several wear tests using the 20 N normal load were performed at different locations on the surface of the repair. Fig. 7b,c shows the σ_X values corresponding to each double wear track.

For the reference points (i.e., those representative of the pristine state), lower compressive RS were measured in Strat 0° than in Strat 67°. This is not in good agreement with the results shown in Fig. 5 and 6. Some repeatability issues of the LMD processing are suspected to impact the RS state between different batches. In addition, a RS redistribution could occur in the coatings as a result of the wear tests.

After the samples were worn with a normal load of 20 N, the RS is redistributed to higher compressive RS (around -600 MPa instead of about -50 MPa and -400 measured at the reference points for Strat 0° and 67° respectively) at 22 µm in depth. A similar progressive increase in compressive RS is observed with increasing depth. Therefore, the RS redistribution induced using 20 N is considered independent of the strategy and of the location of the wear tests. Increasing the normal load to 50 N further increases the compressive RS and changes the RS profile along the depth. For instance, in the case of Strat 67°, a magnitude of around -660 MPa is maintained at a depth of 64 µm. Concerning the Strat 0° sample, a similar trend can be observed, with -550 MPa RS being measured at 92 µm. Such value is higher than the RS at the equivalent depth after the 20 N tests. Interestingly, the 5 N test produces even higher compressive RS at 22 µm, indicating a tendency to localize the wear damage closer to the free surface with decreasing the normal load [44]. The Strat 0° results show overall higher scatter. Such scatter is ascribed to a higher heterogeneity induced by the 0° scanning strategy.

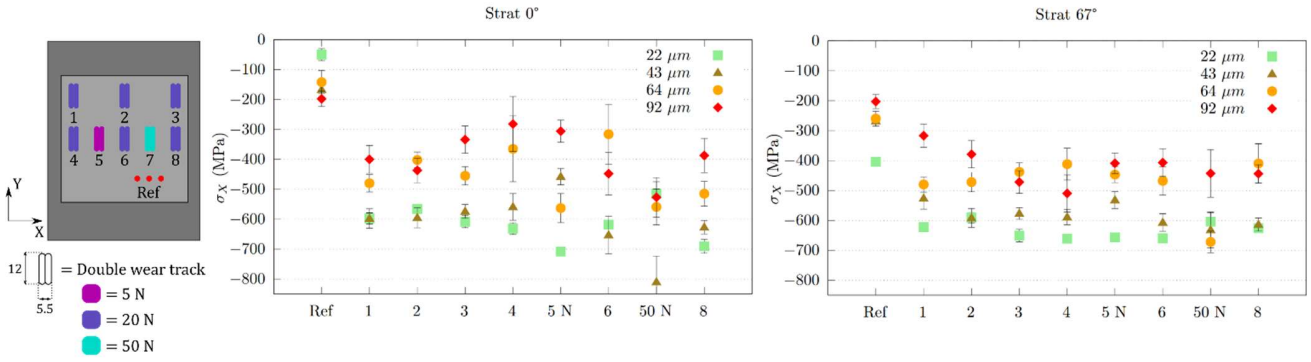

Fig. 7 (a) Schematic illustration of the location of the double wear tracks over the sample surface; dimensions are shown in millimeters. Plots showing the σ_X values corresponding to the as-milled material (Ref), as well as to each double wear track for (b) the Strat 0° sample and (c) the Strat 67° sample.

3.4. Wear volume of LMD repaired parts

Reciprocating sliding wear tests (with an applied load of 20 N) were used to create wear scars at different positions on both samples (as shown in Fig. 8a). Those tests were performed on the XRD-analyzed samples shown in Fig. 5. The wear tests were performed from the right edge to the middle of the repair (negative direction of the X-axis, Fig. 8b). The plots shown in Figs. 8c-f combine the RS state at 22, 43, and 64 µm and the wear volume profiles of the two samples. A flat wear volume profile is observed for the Strat 0° sample. In this case, the RS state along the Y component varies over the sample surface (from -650MPa to -350MPa) and does not show any clear correlation with the wear volume. Also, in order to test the repeatability of the wear tests, two wear profiles (i.e., using two different samples) were performed for the Strat 67° sample.

The first wear volume profile (black line) reveals a decrease toward the center of the repair, in agreement with the trend observed in the σ_Y profile: higher compressive RS leads to lower wear volumes (from 1.42 mm^3 to 1.22 mm^3). However, the second wear profile (blue line) in Fig. 8e,f has a scattered trend that does not correspond to any RS profile. Interestingly, such RS profile correlates better with the wear volume profile measured for the Strat 0° sample.

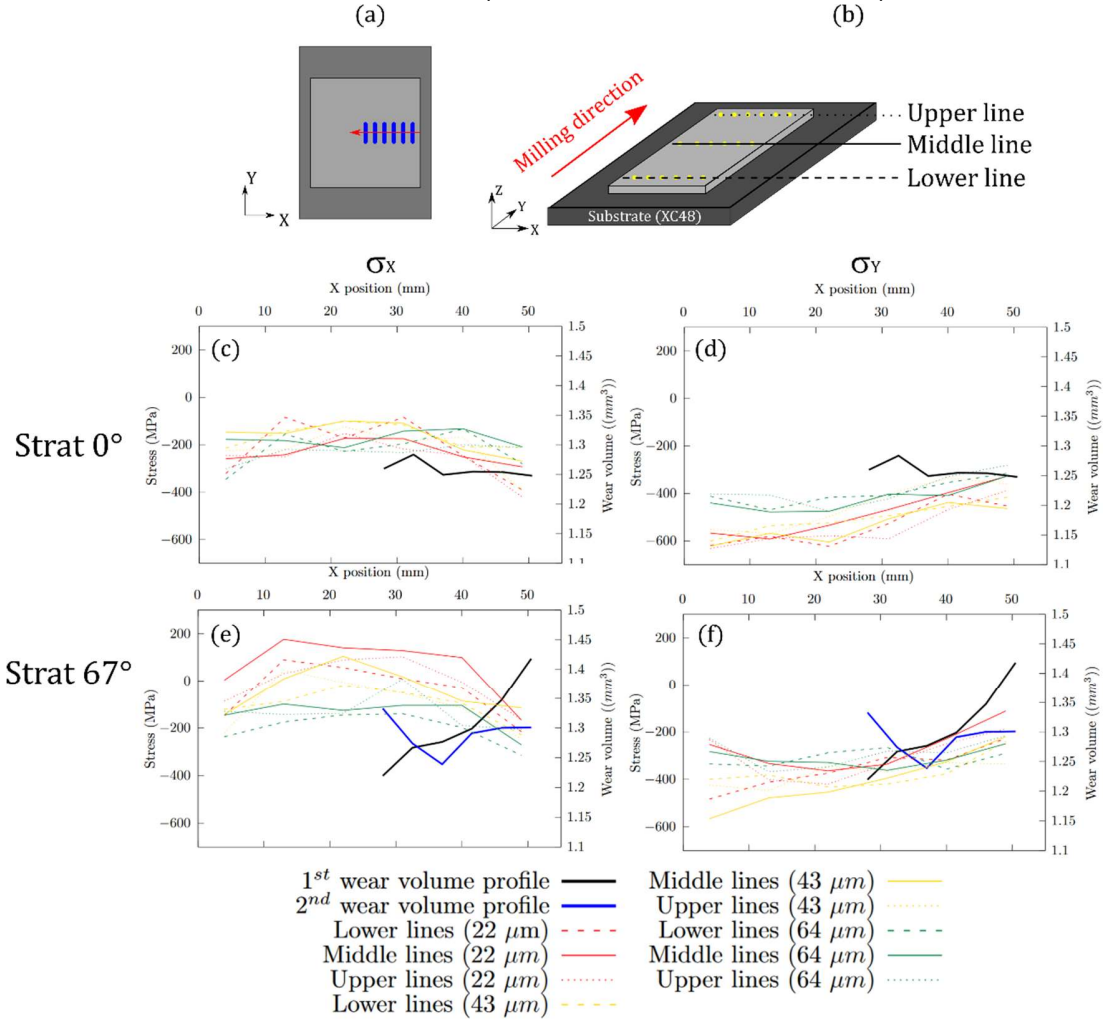

Fig. 8 Schematic illustrations describing (a) the location of the wear volume tests and (b) the location of the RS lines over the sample surface. Plots showing the RS principal components and wear profiles against the location for (c) and (d) the Strat 0° and (e) and (f) the Strat 67° scanning strategies.

After performing wear tests of 5,000 cycles, it is observed that the main wear mechanisms are abrasion and adhesion, as cold-welded debris are observed adhered to the surface. Multiple grooves are also observed; they are most likely dug out by debris (Fig. 9a). It is worth noting that the mechanisms are the same regardless of the load applied and the scanning strategy. In addition, it is observed that the Strat 67° sample wears, on average, slightly more than the Strat 0° one (Fig. 9b). Despite the small difference in terms of wear volume (1.26 to 1.29 mm^3), the standard deviation of wear volume of the Strat 67° sample is considerably higher. This difference implies a less strong influence of RS on the wear behavior in the Strat 67° sample. However, after subsequently performing another 5,000 cycles to each wear track, the two types of samples exhibit similar amount of volume loss (around 1.23 mm^3). This phenomenon is attributed to the relaxation of the initial RS state.

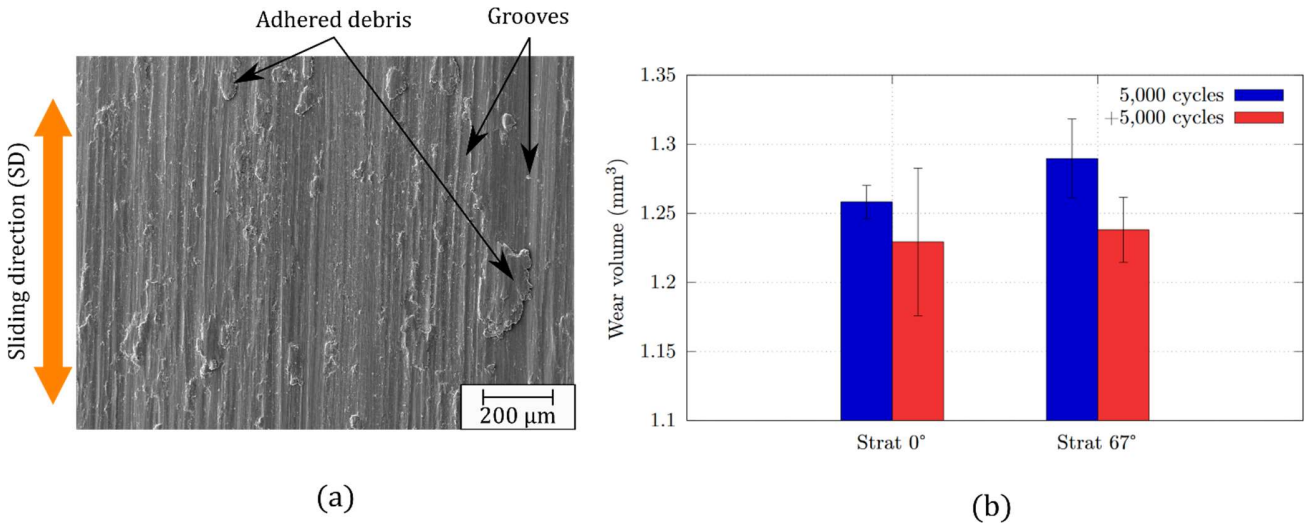

Fig. 9 (a) Representative SEM image of the interior of one the wear tracks performed on the Strat 0° samples after the first 5,000 cycles. (b) Plot showing the mean wear volume calculated from every wear profile after the first 5,000 cycles, and after an additional +5,000 cycles

4. Discussion

The sliding wear behavior of metals is mainly controlled by the hardness. Conventionally, IN718 undergoes a homogenization plus double aging heat treatment (1065°C x 1.5h/air cooling + 760°C x 10h/furnace cooling + 650°C x 8h/air cooling) to achieve microstructural stability and optimal mechanical properties [45]. Such heat-treatments relax the internal stresses and enable the precipitation of the hardening phases γ‘ and γ“ [46]. Yet, even without precipitation of hardening phases, our as-built samples exhibit a high hardness (Fig. 4b,d). This is due to the presence of sub-grain cellular solidification structures. Such structures possess a high amount of dislocation because of the high cooling rate inherent to the LMD process [47]. As shown in Fig. 3b, the high amount of defect leads to grains with strong misorientation inside the as-built microstructure. From 100µm below the surface, such substructures are not affected by the milling.

According to the literature, repairs with low height (2 mm before being milled) induce compressive RS [48]. We observe such trend also on our data. In addition, milling the repair part influences the microstructure and the RS at the surface and subsurface [49], [50]. As observed in Fig. 6, it is considered that milling mainly increases the compressive RS [51], [52] and spatially redistributes the RS at the lower depths (<90 µm). The fact that the Strat 0° sample has higher RS than the Strat 67° one is well established in the literature [20], [21], [41], [53]. A more homogeneous heat flux is developed when applying a 67° rotation of the laser path direction. This heat dissipation induces lower RS. As the same milling parameters were used (Table 2) on the two types of samples, the difference in terms of RS magnitude would be caused by the scanning strategy. The maximum compressive RS values are measured in the Strat 0° sample along the Y-direction, i.e. parallel to the scanning direction. So far, contradictory results are reported in the literature about the largest build-plane principal RS because of the influence of the geometry of the part [54] on the RS values. The milling process used in this study would impact the RS magnitudes but is not expected to affect the general RS distribution of the original as-built samples.

SXEDD measurements within the worn tracks showed that the distributions of the compressive RS depth profiles induced by the reciprocating sliding test depend on the load. The redistribution of the initial RS state to higher compressive RS along the sliding direction has been previously observed [55], [56]. In our case, when the normal load was increased to 50 N, higher compressive RS were induced at higher depths (92 µm). This fact indicates that the higher the load, the deeper the microstructure of the coatings is affected. It is highly likely that, because of the high initial amount of dislocation, the hardening induced by the reciprocating wear test is fast. It is therefore assumed that the high compressive residual stresses are induced rapidly after the start of the wear tests. Importantly, these results indicate that the initial RS state would have a negligible influence on the final wear-induced RS state. In fact, all wear tests on both types of samples induced RS (X component) values of -600 MPa at 22 µm depth. It must be noted that because of the sufficiently large thickness of the

repair, the substrate material is not affected by the wear tests. For such thicknesses of the repair, the material of the substrate (XC48) does not impact the wear results. In fact, in dry-contact sliding conditions and at the applied pressure, the maximum shear occurs near the surface, i.e., far from the repair/substrate interface [57].

On the contrary, Fig. 9 indicates that the overall worn volume of each scanning strategy is influenced by the initial RS state. The Strat 67° sample wears slightly more than the Strat 0° sample after 5,000 cycles. The main difference between the two samples is the stress along the X-direction at 22 µm. Such stress is tensile (Fig. 5) in the Strat 67° sample but compressive in the Strat 0° sample. Tensile RS may facilitate wear debris delamination at the early stages of wear. On the contrary, compressive RS may delay crack propagation and consequently decrease the amount of debris detached from the surface. The reduced magnitude of σ_Y in Strat 67° compared to Strat 0° might also explain the wear volume difference. As one of the main wear mechanisms is abrasion, if a lower amount of debris occurs inside the contact, the plowing wear will be reduced. We also observe that after 5,000 cycles, the same compressive RS state is induced at the surface/subsurface of the repaired material. Thus, the differences in the initial RS state would impact the wear performances only at the very early stages of wear.

After performing additional 5,000 cycles of wear, the difference in volume loss between the two samples vanishes because of the similar compressive state induced at the beginning of the wear tests. Moreover, it is worth noting that the slight difference in terms of porosity (Fig. 4) between the two samples has a negligible influence on the wear volume. This conclusion is based on the fact that, firstly, cracks initiating from pores are not observed via SEM, and secondly, if pores would affect the volume loss, measured wear volume values would have been much more scattered leading to even bigger standard deviations. In addition, high plastic deformation might reduce the size of pores, limiting their impact on wear [58].

The length and width of the samples used in this study are significantly longer than the height. This ratio results in a weak accumulation of heat during the repair. The good heat dissipation reduces the occurrence of epitaxial growth of the grains. Consequently, the two printing strategies yield similar microstructure, hardness, and density. Such similar features are most likely the reason why the wear behavior is similar. As it has been shown in the literature, texture and grain size might impact wear [24], [59]. Hence, the results shown in this work should not be generalized to the conclusion that repairing using the Strat 0° scanning strategy will reduce wear. Larger repair heights are expected to severely increase the texture in the case of the Strat 0° samples [53], [60], leading to remarkable microstructural differences between the two investigated scanning strategies. Furthermore, larger repair heights are also expected to change the nature of RS from compressive to tensile at the surface/subsurface [48]. Such speculations certainly represent subjects for further work.

5. Conclusions

The influence of the RS state on the wear behavior of as-milled LMD IN718 samples was investigated on two different laser scanning strategies, one where the laser direction changed by 67° at each successive layer (Strat 67°) and one where the laser scanning direction was kept constant (Strat 0°). The Strat 67° scanning strategy yields overall lower compressive RS than the Strat 0° scanning strategy. Sliding tests further increase the original compressive RS on both samples. The extent of the increase along the depth is determined by the normal load applied during the wear tests: higher loads lead to higher depths being affected. Moreover, some impact of the scanning strategy on the wear resistance was observed. Due to the lower initial compressive RS along the sliding direction and tensile RS perpendicular to it, the Strat 67° sample is more prone to wear at the initial stages (first 5,000 cycles). It is argued that the RS in the as-milled state does not significantly impact the sliding wear resistance, because the sliding process leads to equivalent compressive RS at both the surface and the subsurface of the worn area.

Acknowledgements

We acknowledge DESY (Hamburg, Germany), a member of the Helmholtz Association HGF, for the provision of experimental facilities. Parts of this research were carried out at PETRAIII. Beamtime was allocated for proposal I-2022025.

Author contributions

The conceptualization and the manufacturing of the samples were done by TZ. The characterization of the materials was performed by TZ. The XRD measurements were performed by TZ, ISM, TM, GAF, and SD. TZ, ISM, GB, EC and TM evaluated and discussed the XRD results. TZ, ISM, and TM wrote the first draft. The manuscript was revised by EC, VF, GAF, SD, and GB. The funding acquisition was done by EC.

Funding

This research work was founded by the *Direction Générale de l'Armement* (DGA, France) and by the *Société Générale des Chemins de fer Français* (SNCF, France).

Conflicts interests or competing interests

The authors declare no competing interests

Data and code availability

The datasets used and/or analysed during the current study available from the corresponding author on reasonable request.

Supplementary information (NotApplicable)

Ethical approval (NotApplicable)

References

[1] P. Liu, Y. Quan, J. Wan, and L. Yu, "Experimental investigation on the wear and damage behaviors of machined wheel-rail materials under dry sliding conditions," *Materials (Basel).*, vol. 14, no. 3, pp. 1–21, 2021, doi: 10.3390/ma14030540.

[2] D. Tejero-Martin, M. Rezvani Rad, A. McDonald, and T. Hussain, *Beyond Traditional Coatings: A Review on Thermal-Sprayed Functional and Smart Coatings*, vol. 28, no. 4. Springer US, 2019.

[3] N. Curry, N. Markocsan, L. Östergren, X. H. Li, and M. Dorfman, "Evaluation of the lifetime and thermal conductivity of dysprosia-stabilized thermal barrier coating systems," *J. Therm. Spray Technol.*, vol. 22, no. 6, pp. 864–872, 2013, doi: 10.1007/s11666-013-9932-9.

[4] B. Graf, A. Gumenyuk, and M. Rethmeier, "Laser Metal Deposition as Repair Technology for Stainless Steel and Titanium Alloys," *Phys. Procedia*, vol. 39, pp. 376–381, 2012, doi: 10.1016/j.phpro.2012.10.051.

[5] Rahito, D. A. Wahab, and A. H. Azman, "Additive manufacturing for repair and restoration in remanufacturing: An overview from object design and systems perspectives," *Processes*, vol. 7, no. 11, 2019, doi: 10.3390/pr7110802.

[6] L. Li, "Advances and characteristics of high-power diode laser materials processing," *Opt. Lasers Eng.*, vol. 34, no. 4–6, pp. 231–253, 2000, doi: 10.1016/S0143-8166(00)00066-X.

[7] M. Prager and C. S. Shira, "Welding of precipitation-hardening nickel- base alloys(Welding precipitation hardenable Ni base alloys noting heat treatment, microfissuring, strain age cracking and other intricacies)," *Weld. Res. Counc. Bull.*, no. 128, 1968.

[8] M. D. Sangid *et al.*, "Role of heat treatment and build orientation in the microstructure sensitive deformation characteristics of IN718 produced via SLM additive manufacturing," *Addit. Manuf.*, vol. 22, pp. 479–496, 2018, doi: https://doi.org/10.1016/j.addma.2018.04.032.

[9] J. M. Wilson, C. Piya, Y. C. Shin, F. Zhao, and K. Ramani, "Remanufacturing of turbine blades by laser direct deposition with its energy and environmental impact analysis," *J. Clean. Prod.*, vol. 80, pp. 170–178, 2014, doi: 10.1016/j.jclepro.2014.05.084.

[10] G. Bi and A. Gasser, “Restoration of nickel-base turbine blade knife-edges with controlled laser aided additive manufacturing,” *Phys. Procedia*, vol. 12, no. PART 1, pp. 402–409, 2011, doi: 10.1016/j.phpro.2011.03.051.

[11] T. Ünal-Saewe, L. Gahn, J. Kittel, A. Gasser, and J. H. Schleifenbaum, “Process development for tip repair of complex shaped turbine blades with IN718,” *Procedia Manuf.*, vol. 47, no. 2019, pp. 1050–1057, 2020, doi: 10.1016/j.promfg.2020.04.114.

[12] X. Wu, W. Zhu, and Y. He, “Deformation prediction and experimental study of 316l stainless steel thin-walled parts processed by additive-subtractive hybrid manufacturing,” *Materials (Basel).*, vol. 14, no. 19, 2021, doi: 10.3390/ma14195582.

[13] K. Kempen, B. Vrancken, S. Buls, L. Thijs, J. Van Humbeeck, and J. P. Kruth, “Selective Laser Melting of Crack-Free High Density M2 High Speed Steel Parts by Baseplate Preheating,” *J. Manuf. Sci. Eng. Trans. ASME*, vol. 136, no. 6, 2014, doi: 10.1115/1.4028513.

[14] S. Chen, H. Gao, Y. Zhang, Q. Wu, Z. Gao, and X. Zhou, “Review on residual stresses in metal additive manufacturing: formation mechanisms, parameter dependencies, prediction and control approaches,” *J. Mater. Res. Technol.*, vol. 17, pp. 2950–2974, 2022, doi: 10.1016/j.jmrt.2022.02.054.

[15] G. Riccardo, B. Rivolta, C. Gorla, and F. Concli, “Cyclic behavior and fatigue resistance of AISI H11 and AISI H13 tool steels,” *Eng. Fail. Anal.*, vol. 121, no. September 2020, p. 105096, 2021, doi: 10.1016/j.engfailanal.2020.105096.

[16] G. Telasang, J. Dutta Majumdar, N. Wasekar, G. Padmanabham, and I. Manna, “Microstructure and Mechanical Properties of Laser Clad and Post-cladding Tempered AISI H13 Tool Steel,” *Metall. Mater. Trans. A Phys. Metall. Mater. Sci.*, vol. 46, no. 5, pp. 2309–2321, 2015, doi: 10.1007/s11661-015-2757-z.

[17] C. Li, Z. Y. Liu, X. Y. Fang, and Y. B. Guo, “Residual Stress in Metal Additive Manufacturing,” *Procedia CIRP*, vol. 71, pp. 348–353, 2018, doi: 10.1016/j.procir.2018.05.039.

[18] E. Beevers *et al.*, “Fatigue properties and material characteristics of additively manufactured AlSi10Mg – Effect of the contour parameter on the microstructure, density, residual stress, roughness and mechanical properties,” *Int. J. Fatigue*, vol. 117, no. July, pp. 148–162, 2018, doi: 10.1016/j.ijfatigue.2018.08.023.

[19] P. Pant *et al.*, “A study of the influence of novel scan strategies on residual stress and microstructure of L-shaped LPBF IN718 samples,” *Mater. Des.*, vol. 214, p. 110386, 2022, doi: 10.1016/j.matdes.2022.110386.

[20] B. Cheng, S. Shrestha, and K. Chou, “Stress and deformation evaluations of scanning strategy effect in selective laser melting,” *Addit. Manuf.*, vol. 12, pp. 240–251, 2016, doi: 10.1016/j.addma.2016.05.007.

[21] M. Carraturo, B. Lane, H. Yeung, S. Kollmannsberger, A. Reali, and F. Auricchio, “Numerical Evaluation of Advanced Laser Control Strategies Influence on Residual Stresses for Laser Powder Bed Fusion Systems,” *Integr. Mater. Manuf. Innov.*, vol. 9, no. 0123456789, 2020, doi: 10.1007/s40192-020-00191-3.

[22] Í. Tomaz, M. Martins, H. Costa, I. Bastos, and M. Fonseca, “Influence of residual stress on the sliding wear of aisi 4340 steel,” *Rev. Mater.*, vol. 25, no. 2, pp. 1–8, 2020, doi: 10.1590/S1517-707620200002.1018.

[23] M. G. Yin, Z. B. Cai, Z. X. Zhang, and W. Yue, “Effect of ultrasonic surface rolling process on impact-sliding wear behavior of the 690 alloy,” *Tribol. Int.*, vol. 147, no. December 2018, p. 105600, 2020, doi: 10.1016/j.triboint.2019.02.008.

[24] Y. Yang, Y. Zhu, M. M. Khonsari, and H. Yang, “Wear anisotropy of selective laser melted 316L stainless steel,” *Wear*, vol. 428–429, no. January, pp. 376–386, 2019, doi: 10.1016/j.wear.2019.04.001.

[25] Y. Yang, X. Li, M. M. Khonsari, Y. Zhu, and H. Yang, “On enhancing surface wear resistance via rotating grains during selective laser melting,” *Addit. Manuf.*, vol. 36, no. September, 2020, doi: 10.1016/j.addma.2020.101583.

[26] M. Bahshwan, C. W. Myant, T. Reddyhoff, and M. S. Pham, “The role of microstructure on wear mechanisms and anisotropy of additively manufactured 316L stainless steel in dry sliding,” *Mater. Des.*, vol. 196, p. 109076, 2020, doi: 10.1016/j.matdes.2020.109076.

[27] Oxford Instruments, “Oxford Instruments.” https://www.oxinst.com/.

[28] C. A. Schneider, W. S. Rasband, and K. W. Eliceiri, “NIH Image to ImageJ: 25 years of image analysis,” *Nat. Methods*, vol. 9, no. 7, pp. 671–675, 2012, doi: 10.1038/nmeth.2089.

[29] Z. Roell, “Zwick Roell,” 2023. https://www.zwickroell.com/products/hardness-testing-machines/.

[30] R. Farla *et al.*, “Extreme conditions research using the large-volume press at the P61B endstation, PETRA III,” *J. Synchrotron Radiat.*, vol. 29, no. 2, pp. 409–423, Mar. 2022, [Online]. Available: https://doi.org/10.1107/S1600577522001047.

[31] J. H. Hubbell and S. M. Seltzer, “NIST Standard Reference Database 126,” *Radiation Physics Division, PML, NIST*, 2004. https://www.nist.gov/pml/x-ray-mass-attenuation-coefficients.

[32] D. Dye, H. J. Stone, and R. C. Reed, “Intergranular and interphase microstresses,” *Curr. Opin. Solid State Mater. Sci.*, vol. 5, no. 1, pp. 31–37, 2001, doi: 10.1016/S1359-0286(00)00019-X.

[33] E. Macherauch, “Das Sin^ 2ψ Verfahren von Rontgenographische Eigenspannungen,” *Z. angew. Phys.*, vol. 13, pp. 305–312, 1961.

[34] M. E. Fitzpatrick, A. T. Fry, P. Holdway, F. A. Kandil, J. Shackleton, and L. Suominen, “Determination of residual stresses by X-ray diffraction.,” 2005.

[35] A. Reuss, “Berechnung der Fließgrenze von Mischkristallen auf Grund der Plastizitätsbedingung für Einkristalle .,” *ZAMM - J. Appl. Math. Mech. / Zeitschrift für Angew. Math. und Mech.*, vol. 9, no. 1, pp. 49–58, Jan. 1929, doi: https://doi.org/10.1002/zamm.19290090104.

[36] P. Haldipur, “Estimation of Single-Crystal Elastic Constants from Ultrasonic Measurements on Polycrystalline Specimens,” *AIP Conf. Proc.*, vol. 1061, no. 2004, pp. 1061–1068, 2004, doi: 10.1063/1.1711735.

[37] M. Wansleben *et al.*, “Photon flux determination of a liquid-metal jet X-ray source by means of photon scattering,” *J. Anal. At. Spectrom.*, vol. 34, no. 7, pp. 1497–1502, 2019, doi: 10.1039/C9JA00127A.

[38] D. Apel, M. Genzel, M. Meixner, M. Boin, M. Klaus, and C. Genzel, “EDDIDAT: A graphical user interface for the analysis of energy-dispersive diffraction data,” *J. Appl. Crystallogr.*, vol. 53, no. 2011, pp. 1130–1137, 2020, doi: 10.1107/S1600576720005506.

[39] Bruker, “Bruker,” 2023. https://www.bruker.com/en/products-and-solutions/test-and-measurement/3d-optical-profilers.html.

[40] W. M. Tucho, P. Cuvillier, A. Sjolyst-Kverneland, and V. Hansen, “Microstructure and hardness studies of Inconel 718 manufactured by selective laser melting before and after solution heat treatment,” *Mater. Sci. Eng. A*, vol. 689, no. February, pp. 220–232, 2017, doi: 10.1016/j.msea.2017.02.062.

[41] I. Serrano-Munoz *et al.*, “The residual stress in as-built Laser Powder Bed Fusion IN718 alloy as a consequence of the scanning strategy induced microstructure,” *Sci. Rep.*, vol. 10, no. 1, pp. 1–15, 2020, doi: 10.1038/s41598-020-71112-9.

[42] S. A. David and J. M. Vitek, “Correlation between solidification parameters and weld microstructures,” *Int. Mater. Rev.*, vol. 34, no. 1, pp. 213–245, 1989, doi: 10.1179/imr.1989.34.1.213.

[43] F. Xiong *et al.*, “Grain growth prediction in selective electron beam melting of Ti-6Al-4V with a cellular automaton method,” *Mater. Des.*, vol. 199, p. 109410, 2021, doi: 10.1016/j.matdes.2020.109410.

[44] H. Hertz, “Ueber die Berührung fester elastischer Körper.,” *J. für die reine und Angew. Math.*, vol. 92, pp. 156–171, 1882.

[45] X. Li *et al.*, “Improved plasticity of Inconel 718 superalloy fabricated by selective laser melting through a novel heat treatment process,” *Mater. Des.*, vol. 180, p. 107915, 2019, doi: https://doi.org/10.1016/j.matdes.2019.107915.

[46] E. M. Fayed, M. Saadati, D. Shahriari, V. Brailovski, M. Jahazi, and M. Medraj, “Effect of homogenization and solution treatments time on the elevated-temperature mechanical behavior of Inconel 718 fabricated by laser powder bed fusion,” *Sci. Rep.*, vol. 11, no. 1, pp. 1–17, 2021, doi: 10.1038/s41598-021-81618-5.

[47] K. M. Bertsch, G. Meric de Bellefon, B. Kuehl, and D. J. Thoma, “Origin of dislocation structures in an additively manufactured austenitic stainless steel 316L,” *Acta Mater.*, vol. 199, pp. 19–33, 2020, doi: 10.1016/j.actamat.2020.07.063.

[48] R. J. Moat, A. J. Pinkerton, L. Li, P. J. Withers, and M. Preuss, “Residual stresses in laser direct metal deposited Waspaloy,” *Mater. Sci. Eng. A*, vol. 528, no. 6, pp. 2288–2298, 2011, doi: 10.1016/j.msea.2010.12.010.

[49] D. Weber *et al.*, “Analysis of machining-induced residual stresses of milled aluminum workpieces, their repeatability, and their resulting distortion,” *Int. J. Adv. Manuf. Technol.*, vol. 115, no. 4, pp. 1089–1110, 2021, doi: 10.1007/s00170-021-07171-7.

[50] Y. Yang, Y. Gong, S. Qu, B. Xin, Y. Xu, and Y. Qi, “Additive/subtractive hybrid manufacturing of 316L stainless steel powder: Densification, microhardness and residual stress,” *J. Mech. Sci. Technol.*, vol. 33, no. 12, pp. 5797–5807, 2019, doi: 10.1007/s12206-019-1126-z.

[51] F. Careri, S. Imbrogno, D. Umbrello, J. C. Outeiro, and A. C. Batista, “A Residual Stress Prediction of Machining IN718 Produced by Direct Energy Deposition,” *Procedia CIRP*, vol. 102, pp. 13–18, 2021, doi: 10.1016/j.procir.2021.09.003.

[52] Y. Liu *et al.*, “Numerical and experimental investigation of tool geometry effect on residual stresses in orthogonal machining of Inconel 718,” *Simul. Model. Pract. Theory*, vol. 106, no. September 2020, p. 102187, 2021, doi: 10.1016/j.simpat.2020.102187.

[53] I. Serrano-Munoz *et al.*, “Scanning Manufacturing Parameters Determining the Residual Stress State in LPBF IN718 Small Parts,” *Adv. Eng. Mater.*, 2021, doi: 10.1002/adem.202100158.

[54] J. Schröder *et al.*, “Diffraction-Based Residual Stress Characterization in Laser Additive Manufacturing of Metals,” *Metals (Basel).*, pp. 1–34, 2021, doi: 10.3390/met11111830.

[55] J. W. Ho, C. Noyan, J. B. Cohen, V. D. Khanna, and Z. Eliezer, “Residual stresses and sliding wear.,” *Wear*, vol. 84, pp. 183–202, 1982, doi: 10.1016/0043-1648(83)90263-6.

[56] D. Mairey, J. E. Sprauel, M. Chuard, and J. Mignot, “Study of residual stresses induced by sliding wear,” *J. Tribol.*, vol. 107, no. 2, pp. 195–199, 1985, doi: 10.1115/1.3261019.

[57] H. Fereidouni, S. Akbarzadeh, and M. M. Khonsari, “The Relation Between Subsurface Stresses and Useful Wear Life in Sliding Contacts,” *Tribol. Lett.*, vol. 68, no. 1, pp. 1–13, 2020, doi: 10.1007/s11249-019-1246-8.

[58] H. Li, M. Ramezani, and Z. W. Chen, “Dry sliding wear performance and behaviour of powder bed fusion processed Ti – 6Al – 4V alloy,” *Wear*, vol. 440–441, no. October, p. 203103, 2019, doi: 10.1016/j.wear.2019.203103.

[59] M. Bahshwan, M. Gee, J. Nunn, C. W. Myant, and T. Reddyhoff, “In situ observation of anisotropic tribological contact evolution in 316L steel formed by selective laser melting,” *Wear*, vol. 490–491, no. November 2021, p. 204193, 2022, doi: 10.1016/j.wear.2021.204193.

[60] N. Nadammal *et al.*, “Critical role of scan strategies on the development of microstructure, texture, and residual stresses during laser powder bed fusion additive manufacturing,” *Addit. Manuf.*, vol. 38, no. December 2020, p. 101792, 2021, doi: 10.1016/j.addma.2020.101792.